PHYSICAL REVIEW B **86**, 045114 (2012)

Real-time real-space TD-DFT for atoms: Benchmark computations on a nonspherical logarithmic grid

C. S. Cucinotta,[1] D. Hughes,[2] and P. Ballone[2]
[1]*School of Physics and CRANN, Trinity College, College Green Dublin 2, Ireland*
[2]*School of Mathematics and Physics, Queen's University Belfast, Belfast BT7 1NN, United Kingdom*

(Received 22 April 2012; published 13 July 2012)

We present the results of benchmark, all-electron computations for the optical properties of atoms with up to 30 electrons, carried out within the adiabatic local density approximation (ALDA) of time-dependent density functional theory. Following the original approach proposed by Janak and Williams, Phys. Rev. B **23**, 6301 (1981), Kohn-Sham orbitals are tabulated on a logarithmic mesh along a discrete set of rays coming out of the atomic nucleus, selected in such a way to accurately represent the angular dependence of ground and excited states. Optical properties are obtained by real-time propagation of the electronic states represented on an extended basis of filled and empty Kohn-Sham orbitals. As expected, the comparison with experimental results is affected by the known drawbacks of the ALDA method. We apply the computational tool to carry out a real-time simulation of Auger processes, whose results, once again, highlight basic (but expected) limitations of the TD-DFT-ALDA approach. We define a novel set of atomic-like basis functions (response functions) meant to optimize the convergence of time-dependent computations, and we measure their performance by comparison with the results of the benchmark computations.

DOI: 10.1103/PhysRevB.86.045114　　PACS number(s): 31.15.ee, 78.20.Bh, 32.30.−r, 32.80.Hd

I. INTRODUCTION

The interaction of light with electrons in atoms, molecules, and solids is arguably the most fundamental experimental technique to probe the electronic properties of condensed matter systems.[1] Nowadays, optical spectroscopy is extensively used to investigate the properties of increasingly complex systems, from macromolecules of biological interest to artificial nanostructures. The link between measured optical properties and the underlying electronic and geometrical structure is established by a variety of theoretical and computational methods, ranging from semiempirical to fully *ab initio* approaches. Among these methods, time-dependent density functional theory[2,3] (TD-DFT) often provides the best compromise of simplicity and accuracy, and for this reason, it is being extensively used for a wide variety of applications.

Within TD-DFT, many-body effects on the time evolution are summarised by the so-called exchange-correlation potential $v_{\text{xc}}(\mathbf{r},t)$, whose detailed expression and properties are still largely unknown.[4] Simple and computationally appealing approaches such as the adiabatic local density approximation (ALDA), however, provide results for optical properties in acceptable, and sometimes remarkable agreement with experimental results, especially for systems of finite dimensions.[5,6]

While TD-DFT is a general theory for the dynamics of the electron density covering a wide range of phenomena and spectroscopic domains, linear-response TD-DFT methods able to compute optical properties such as the absorption spectrum, directly comparable to experimental data, have been developed and validated by several groups[7,8] and are now extensively used for applications.[9] Most of these methods do not explicitly involve the time variable and provide directly energies or, equivalently, frequencies, of optical excitations.

Real-time real-space methods[10] going beyond the linear-response regime have also been developed and implemented in computer codes,[11,12] providing, in principle, a more comprehensive and intuitive view of the system evolution. The corresponding frequency-dependent representation of optical properties is obtained from the Fourier transform of the time-correlation function for the oscillating dipole moment.[10]

At present, the most fundamental open issues for TD-DFT concern the functional form of $v_{\text{xc}}(\mathbf{r},t)$ beyond ALDA. Less fundamental, but equally important problems concern computational aspects, and, in particular, the choice of the representation for the single-particle orbitals and electron density, the framework to extract optical properties from the TD-DFT equations, and the choice of the algorithm to integrate the time evolution equations.

Popular computational implementations of TD-DFT are based on discrete basis sets, and on numerical grids. Discrete basis sets, in particular, include Gaussian, Slater and numerical (atomic-like) functions as well as plane waves. Finite differences and finite elements[13] have been used for grid-based implementations, and the usage of wavelets[14] has been considered by a few groups.[15] In most cases, TD-DFT computations are carried out in the pseudopotential approximation, including explicitly in the computations only valence electrons. A relevant exception is represented by pseudospectral methods implemented for atoms and small molecules.[16,17]

The expanding role of TD-DFT and the ongoing search for better approximations to the exact but unknown TD-DFT functional emphasise, the need for simple yet relevant test cases,[18] and for a numerical framework able to provide a quantitative assessment of advantages and limitations of different schemes unaffected by computational uncertainties. Among systems of finite dimension, atoms represent an appealing testing ground,[19] partly because of their limited size and complexity, and even more because of the wealth of exact or nearly exact information on their properties provided by experiments[20] and computations.[21] Moreover, accurate grid representations of atomic orbitals have been developed long ago[22] and within the density functional (DF) framework,[23] they have been thoroughly tested for ground-state properties.[24]

Despite these considerations, only a limited number of systematic TD-DFT studies of atoms have been reported, and in several cases, crucial computational details such as the basis set, the real-space grid, or the real-time integration algorithm, and convergence parameters have not been specified. As a result, the potential of atoms for TD-DFT testing and development purposes has been greatly underexploited by the condensed matter computational community.

The aim of our study is twofold. First of all, we implement and test a grid method for atoms first introduced many years ago by Janak and Williams.[25] The method is able to deal with nonspherical atoms and represents the radial dependence of KS orbitals on a logarithmic mesh and thus is suitable for all-electron computations. While nonsphericity is the exception for ground-state densities, it is the norm for atoms in an external field. The method of Janak and Williams, therefore, represents an appealing tool to investigate optical excitation in atoms, since it provides a computational framework free of shape approximations, approaching full convergence in the real-space representation of orbitals, and still retaining many of the familiar features of ground-state atomic computations. Our second aim, therefore, is to validate the method of Janak and Williams for TD-DFT computations of atomic excited-state properties. To focus the attention on the computational part, we limit our analysis to the local spin density, ALDA exchange and correlation approximations, even though, to some extent, this approach has been superseded by more refined approximations in practical computations.[18]

The results of our simulations agree with the general picture extensively discussed in the literature. First of all, TD-DFT-ALDA is able to predict fairly accurately the excitation spectrum of light atoms far from shell and subshell closures. In several cases, however, the ALDA scheme introduces apparent artifacts in the absorption spectrum, due to the well-known underestimation of electron binding by the underlying local spin density approximation. Despite this important problem, related to the choice of the exchange-correlation potential, the computational method described in our paper displays a remarkable degree of stability, accuracy, and efficiency. A strategy to enhance these positive features of our approach is discussed in Appendix, where we introduce a set of optimally localized functions, able to provide converged results already with a very limited size of the basis set. This last method has a clear relation with the response function approach of Refs. 26 and 27.

To emphasise the capabilities of the method, in the last part of the paper, we apply our computational tool to simulate Auger processes in relatively light atoms. Real-time real-space simulations spectacularly fail to reproduce the physical process, apparently because TD-DFT-ALDA does not contain a quantized representation of the electromagnetic field, and even electron quantization is reproduced only at the mean-field level. Even though the simulation results are not very surprising, they still provide a clear illustration of the ability of our all-electron, nonspherical atom model to characterize the real-time dynamics in a physically relevant many-electron system as described by any specific density functional approximation, thus highlighting its strengths and weaknesses in a direct and intuitive way.

II. THE MODEL AND THE COMPUTATIONAL METHOD

We consider atoms made of N electrons in the Coulomb potential of a pointlike atomic nucleus of charge Z fixed at the origin. Within the density functional approach, the electronic structure of the system is described by N single-electron Kohn-Sham orbitals $\{\psi_i(\mathbf{r}), i = 1, \ldots, N\}$, whose square modulus gives the electron density according to the relation

$$\rho(\mathbf{r}) = \sum_{i=1}^{N} |\psi_i(\mathbf{r})|^2. \tag{1}$$

The ground-state energy and density are determined by minimizing the Kohn-Sham functional,

$$\begin{aligned} E_{\mathrm{KS}}[\rho] = &-\frac{1}{2}\sum_{i=1}^{N}\langle\psi_i(\mathbf{r})|\nabla^2|\psi_i(\mathbf{r})\rangle \\ &+\frac{1}{2}\int\frac{\rho_Q(\mathbf{r})\rho_Q(\mathbf{r}')}{|\mathbf{r}-\mathbf{r}'|}d\mathbf{r}d\mathbf{r}' \\ &+\int V_{\mathrm{ext}}(\mathbf{r})\rho(\mathbf{r})d\mathbf{r} + U_{\mathrm{XC}}[\rho], \end{aligned} \tag{2}$$

with respect to the KS orbitals. In the equation above, $\rho_Q(\mathbf{r}) = Z\delta(\mathbf{r}) - \rho(\mathbf{r})$, $V_{\mathrm{ext}}(\mathbf{r})$ represents any static external perturbation to the atom,[28] and U_{XC} gives the so-called exchange correlation (XC) energy. Atomic Hartree units are used throughout the paper. Relativistic effects are neglected. For the sake of simplicity, in what follows, we consider only the local spin density (LSD) approximation.[29]

The minimum condition under the constraint of a fixed number of electrons is expressed by the self-consistent Euler-Lagrange equations:

$$\begin{aligned} &\left[-\frac{1}{2}\nabla^2 + \int\frac{\rho_Q(\mathbf{r}')}{|\mathbf{r}-\mathbf{r}'|}d\mathbf{r}' + V_{\mathrm{ext}}(\mathbf{r}) + \mu_{\mathrm{XC}}(\mathbf{r})\right]\psi_i(\mathbf{r}) \\ &\quad = \left[-\frac{1}{2}\nabla^2 + V_{\mathrm{KS}}(\mathbf{r})\right]\psi_i(\mathbf{r}) = \epsilon_i\psi_i(\mathbf{r}), \end{aligned} \tag{3}$$

where $\mu_{\mathrm{XC}}(\mathbf{r}) = \delta U_{\mathrm{XC}}/\delta\rho(\mathbf{r})$, and the Kohn-Sham potential $V_{\mathrm{KS}}(\mathbf{r})$ has been defined as the sum of the external, Hartree, and exchange-correlation terms. To simplify notation, we do not explicitly indicate the (possible) dependence of V_{KS} on the spin σ.

The determination of ground-state properties for atoms is routinely carried out by assuming that the electron density and the KS potential are spherically symmetric. In such a case, KS orbitals can be selected to be eigenstates of the KS Hamiltonian and of rotations around the origin, and thus are written as

$$\psi_{nlm\sigma}(\mathbf{r}) = \frac{\chi_{nl\sigma}(r)}{r}Y_{lm}(\theta,\phi), \tag{4}$$

where Y_{lm} is a spherical harmonics of angular momentum $L^2 = l(l+1)$ and $L_z = m$. Moreover, σ labels the spin ($\pm 1/2$) of the electron occupying the orbital. For every (l,m) value, different principal quantum numbers n correspond to different numbers of radial nodes ($= n - l - 1$). In what follows, the n, l, and σ quantum number are collectively denoted by $\nu = \{nl\sigma\}$.

The radial function $\chi_\nu(r)$ satisfies the equation

$$\frac{d^2\chi_\nu(r)}{dr^2} + \left\{2[\epsilon_\nu - V_{\mathrm{KS}}(r)] - \frac{l(l+1)}{r^2}\right\}\chi_\nu(r) = 0, \tag{5}$$

which has to be solved with the boundary conditions

$$\lim_{r \longrightarrow 0} \chi_\nu(r) = A r^{l+1}[1 + \eta r + \mathcal{O}(r^2)], \tag{6}$$

where A is fixed by normalization, $\eta = -Z/(l+1)$, and

$$\lim_{r \longrightarrow \infty} \chi_\nu(r) = B \exp(-\sqrt{c_\nu} r) \tag{7}$$

with $c_\nu = -2\epsilon_\nu$, upon assuming that $V_{\mathrm{KS}}(r)$ vanishes at large distances. The constant B in the last of these limiting equations is obtained by imposing continuity conditions on $\chi_\nu(r)$ over the entire radial range.

The standard computational approach to determine the atomic ground state represents orbitals on a logarithmic mesh defined by the relation

$$r(x) = r_0 e^{\beta x}, \tag{8}$$

where $0 \leqslant x \leqslant +\infty$ and $0 \leqslant r_0,\ \beta \ll 1$. The change of variables from the linear to the logarithmic mesh is meant to concentrate grid points in the vicinity of the origin and changes the equation satisfied by $\chi_\nu(r)$ into

$$\frac{d^2\chi_\nu(x)}{dx^2} - \beta \frac{d\chi_\nu(x)}{dx} + \beta^2\{2r^2(x)[\epsilon_\nu V_{\mathrm{KS}}(x)] \\ - l(l+1)\}\chi_\nu(x) = 0. \tag{9}$$

The solution is obtained by integrating Eq. (9) outwards and inwards starting from $r = R_{\max}$ and from $r = r_0$, respectively, using the limits specified by Eqs. (6) and (7), and matching the two solutions at an intermediate radius R_{match}.

The electrostatic potential satisfies Poisson's equation

$$\nabla^2 V_H(\mathbf{r}) = -4\pi\rho(\mathbf{r}) \tag{10}$$

and is obtained from the electron density by a computational method closely related to the one used to solve the KS equations.

Benchmark results for the spherically symmetric ground state of atoms from $Z = 1$ to 92 are reported in Ref. 24. Total energy and eigenvalues converged to within 1 μHa can be obtained at a modest computational cost. Nonspherical ground-state configurations may spontaneously arise in open shell atoms whose partially filled level consists of $l > 0$ orbitals, and more, in general, for atoms perturbed by an external potential of lower symmetry.

An elegant method to deal with these cases was proposed long ago by Janak and Williams,[25] based on the representation of KS orbitals on an angular mesh of N_Ω *rays* coming out of the nucleus. Each ray is identified by a pair of (θ_i,ϕ_i) coordinates $(i = 1,\ldots,N_\Omega)$, whose location on the $[0:\pi;0:2\pi]$ domain is selected in such a way to integrate exactly spherical harmonics of up to $l_{\max}$ angular momentum. The $l_{\max}$ value, in turn, is optimized following a 2D Gauss integration approach, that assigns integration weights $\{w_i\}$ to the rays.[30]

A basis set for the KS orbitals covering a range of angular momenta l up to $l_{\max}$ is generated by the following, l-dependent representation of the KS Hamiltonian:

$$\hat{H}_{\mathrm{KS}} = -\tfrac{1}{2}\nabla^2 + V_{\mathrm{KS}} = \hat{H}_l^0 + \delta\hat{H}_l. \tag{11}$$

The two operators $\hat{H}_l^0$ and $\delta\hat{H}_l$ are defined as follows:

$$\hat{H}_l^0 = -\frac{1}{2r}\frac{d^2}{dr^2}\, r + V_{\mathrm{KS}}(\mathbf{r}) + \frac{l(l+1)}{2r^2} \tag{12}$$

and

$$\delta\hat{H}_l = \frac{1}{2r^2}[\langle\hat{r}|\hat{L}^2|\hat{r}'\rangle - l(l+1)\delta(\hat{\mathbf{r}} - \hat{\mathbf{r}}')]. \tag{13}$$

In other terms, $\hat{H}_l^0$ accounts for the radial part of the kinetic energy and for the full KS potential, while $\delta\hat{H}_l$ represents angular contributions to the kinetic energy.

A basis set of functions $|\nu\rangle = \eta_\nu(\mathbf{r},\epsilon_\nu)$ is generated by considering the eigenfunctions of the self-consistent operator $\hat{H}_l^0$ whose behavior close to the origin is given by

$$\lim_{r\to 0} \eta_\nu(\mathbf{r},\epsilon_\nu) = r^l Y_{lm}(\hat{\mathbf{r}}). \tag{14}$$

Here, $\nu = (n,l,m,\sigma)$, since, for nonspherical solutions, these functions depend explicitly on m via Eq. (14). The eigenstates of the full KS Hamiltonian are then expanded in terms of the functions $\eta_\nu(\mathbf{r})$:

$$\psi_i(\mathbf{r}) = \sum_\nu c_\nu^{(i)} \eta_\nu(\mathbf{r},\epsilon_\nu). \tag{15}$$

The expansion coefficients are determined by the linear eigenproblem equations

$$\sum_\nu \langle\nu|\hat{H}_{\mathrm{KS}} - \epsilon|\nu'\rangle c_{\nu'}^{(i)} = 0. \tag{16}$$

In our computer implementation, the functions $\eta_\nu(\mathbf{r},\epsilon_\nu)$ are written, in turn, as

$$\eta_\nu(\mathbf{r},\epsilon_\nu) = \frac{\chi_\nu(\mathbf{r},\epsilon_\nu)}{r} \tag{17}$$

and the χ_ν's are determined, along each radius, using the same method already described for the spherical case. Both in the case of spherical and nonspherical atoms, the procedure introduced to compute occupied states can be used to determine unoccupied orbitals.

In our computations, occupied and unoccupied states are forced to have a node at the boundary of the radial mesh that therefore acts like a hard potential barrier. This, in turn, has the effect of discretizing the spectrum over the entire energy range that otherwise would comprise both localized states of negative eigenvalue, and a continuum of scattering states. In what follows, all computations have been performed using a box of radius $R_{\max} = 25$ a.u. The extension of the logarithmic grid method to nonspherical atoms opens the way to its application to time-dependent phenomena.

According to TD-DFT, the time evolution of an N-electron system subject to a perturbing potential $V_{\mathrm{ext}}(\mathbf{r},t)$ is obtained by integrating the Schroedinger-like equation:[2]

$$i\hbar\frac{\partial\psi_i(\mathbf{r},t)}{\partial t} = \hat{H}_{\mathrm{KS}}\psi_i(\mathbf{r},t), \tag{18}$$

where $\{\psi_i\}$, $i = 1,\ldots,N$ are again single electron orbitals and $\hat{H}_{\mathrm{KS}}$ depends explicitly on time via $V_{\mathrm{ext}}(\mathbf{r},t)$ as well as implicitly via the time dependence of the electron density. A variety of strategies to compute excitation energies and other time-dependent properties for atoms and, in general, for many-electron systems are described in Ref. 5b. An increasingly popular approach is based on the real-time real-space computational description of the electron density evolution under a suitable perturbation.[10] In most cases, the perturbing potential is switched on adiabatically or, at least, continuously, and the ground-state KS orbitals provide the initial condition for the integration of Eq. (18).

The time evolution is carried out by discrete integration of the equations of motion. The time evolution of each orbital $\psi_i(\mathbf{r},t)$, in particular, is expressed in the linear operator form:

$$\psi_i(\mathbf{r},t+\delta t) = \hat{U}(t+\delta t \leftarrow t)\psi_i(\mathbf{r},t), \tag{19}$$

where

$$\hat{U}(t+\delta t \leftarrow t) = \exp\left[-i\int_t^{t+\delta t} d\tau \hat{H}_{\mathrm{KS}}(\tau)\right] \tag{20}$$

that in the limit of small δt, becomes

$$\hat{U}(t+\delta t \leftarrow t) \simeq \exp\left[-i\delta t \hat{H}_{\mathrm{KS}}(t)\right]. \tag{21}$$

In our implementation, we first expand each orbital on a finite basis of atomic-like orbitals $\{\phi_i(\mathbf{r})\}$:

$$\psi_i(\mathbf{r},t) = \sum_j c_j^{(i)}(t)\phi_j(\mathbf{r}), \tag{22}$$

then, the discrete evolution of the expansion coefficients is given by

$$c_j^{(i)}(t+\delta t) = \sum_k U_{jk} c_k^{(i)}(t), \tag{23}$$

where

$$\begin{aligned} U_{ij} &= \langle \phi_i | \hat{U}(t+\delta t \leftarrow t) | \phi_j \rangle \\ &\simeq \langle \phi_i | \exp\left[-i\delta t \hat{H}_{\mathrm{KS}}(t)\right] | \phi_j \rangle \end{aligned} \tag{24}$$

are the elements of the matrix **U** representing the operator $\hat{U}$ on the discrete orbital basis. In the simplest approach, the set of atomic-like functions $\{\phi_i(\mathbf{r})\}$ may consist of occupied and empty KS states for the atom under study. A second and possibly more appealing choice is discussed in Appendix.

The matrix **U** is easily computed in the representation in which the KS Hamiltonian is diagonal. Let us represent the transformation of the Hamiltonian into its diagonal form by the matrix operation:

$$\hat{\mathbf{H}}_{\mathrm{KS}} = \mathbf{V}\,\mathbf{D}\,{}^{\dagger}\mathbf{V}, \tag{25}$$

where **D** is the diagonal form of $\hat{\mathbf{H}}_{\mathrm{KS}}$, **V** is the unitary operator made from the Hamiltonian eigenvectors in the original basis and ${}^{\dagger}\mathbf{V}$ is its Hermitian conjugate. Then,

$$\mathbf{U} = \mathbf{V}[\exp(-i\delta t\mathbf{D})]\,{}^{\dagger}\mathbf{V} \tag{26}$$

and the time evolution operator $\hat{U}(t+\delta t \leftarrow t)$ can be obtained by matrix times matrix multiplications. It turns out that for a basis of up to a few hundred functions, the diagonalization of the KS Hamiltonian $\hat{H}_{\mathrm{KS}}$ can indeed be carried out at each step quickly enough to allow the real-time real-space simulation of atoms over a time span sufficient for a fairly accurate determination of excited states properties.

We apply this technique to compute the dipole absorption spectrum of atoms, using the ALDA approximation to TD-DFT. Starting from the atomic ground state, the computation of the optical properties is carried out by first applying a short-duration perturbation represented by a time-dependent electric field aligned along a fixed direction that we shall call the z axis. Then, the dynamics of the electron density is monitored for times far exceeding the duration of the applied perturbation. In the computations described below, the external field $V_{\mathrm{ext}}(\mathbf{r},t)$ is defined as follows:

$$V_{\mathrm{ext}}(\mathbf{r},t) = \begin{cases} 0, & t < 0, \\ \epsilon V_0(\mathbf{r})\left(1-\cos\frac{2\pi t}{\Delta}\right), & 0 \leqslant t < \Delta, \\ 0, & t > \Delta, \end{cases} \tag{27}$$

where Δ and ϵ are suitable scales for the time and energy of the perturbation, respectively. To prevent instabilities, the dipolar potential has been modified at long range, according to

$$V_0(\mathbf{r}) = ze^{-0.0001r^2} \tag{28}$$

and ϵ in Eq. (27) is limited to values of the order of 10^{-3} a.u.

The integration of the equation of motion allows us to compute the dipole moment **P** at each step, and therefore we can compute the time correlation function:

$$A(\tau) = \langle \mathbf{P}(t+\tau)\mathbf{P}(t)\rangle_t, \tag{29}$$

where $\langle \dots \rangle_t$ indicates averaging with respect to t. The dipole absorption spectrum $S(\omega)$ is computed from the imaginary part $\mathcal{I}[\alpha]$ of the dynamic polarizability $\alpha(\omega)$ according to

$$S(\omega) = \frac{2\omega}{\pi}\mathcal{I}[\alpha(\omega)], \tag{30}$$

where $\alpha(\omega)$ is computed by Fourier transforming $A(\tau)$:

$$\alpha(\omega) = \int_0^{\infty} dt e^{i\omega t} A(t). \tag{31}$$

The quality of the computation, in principle, can be checked by verifying the validity of the f-sum rule:

$$N = \int_0^{\infty} d\omega S(\omega), \tag{32}$$

where N is the number of electrons. In practice, our computations cover an energy range too narrow to satisfy such a sum rule.

In what follows, the logarithmic mesh consists of 2000 grid points stretching from $r_0 = 2 \times 10^{-5}$ a.u. to $R_{\max} = 25$ a.u., corresponding to $\beta = 0.007\,022\,8$ [see Eq. (8)]. The angular mesh comprises 32 points and is able to integrate exactly spherical harmonics of up to $l_{\max} = 9$, largely sufficient for our purposes. A visual impression of the resolution provided by the angular grid can be obtained from Fig. 1 showing a color map of $Y_{9,5}(\theta,\phi)$.

The typical time step used in our computation is 0.01 a.u., or 2.4×10^{-4} fs that, up to $Z = 30$, is sufficiently short to allow the integration of the equations of motion both for core and valence states. Tests have been carried out with shorter time steps, confirming the reliability of the $\delta t = 0.01$ a.u. choice. The perturbing potential is defined by its intensity $\epsilon = 10^{-3}$ a.u. and duration $\Delta = 10$ a.u., equal to 0.24 fs.

The integration of the equation of motion for Ar ($Z = 18$, using 106 basis functions) over 200 000 steps, and covering 48 fs, takes 16 hours on a single Intel Q8300 CPU (2.5 GHz). The computation can be speeded up significantly by introducing a frozen core approximation, or, in other term, by keeping fixed the orbitals of lowest energy to their ground-state value. The code is also suitable for parallelization, even though no effort has been made along this direction. As discussed below,

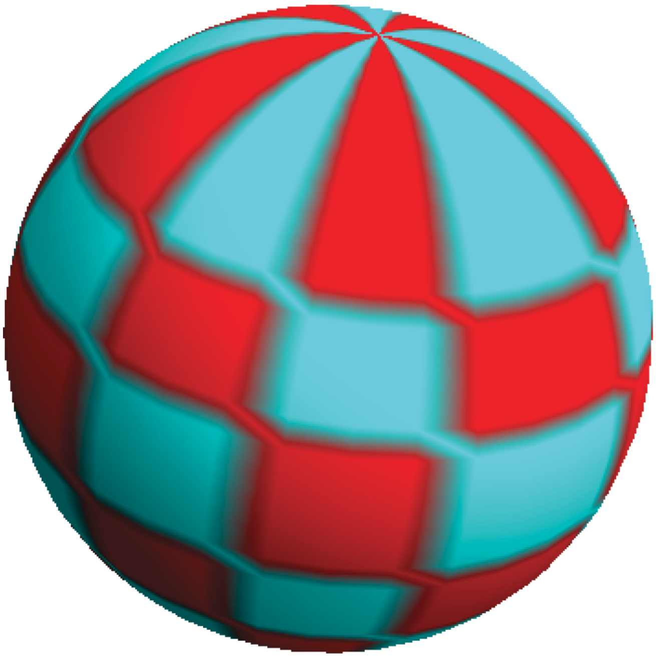

FIG. 1. (Color online) Color map of the $Y_{9,5}$ spherical harmonics. Blue and red regions identify positive and negative patches, respectively.

we used basis sets of filled and empty states as well as *response functions* that are described in Appendix.

III. DIPOLE EXCITATION ENERGY OF ATOMS

Ground-state and optical properties of light atoms with up to 30 electrons (Zn) have been computed by the methods described in the previous section, using the local spin density approximation. To simplify the comparison with previous computations, we focused on atoms such as He, Li, Be, N, Ne, Na, Mg, Ar, Ca, P, and Zn whose ground-state electron density is expected to be spherically symmetric. Computations for H and He within different exchange-correlation approximations have been carried out as well to test the method and its implementation.

For all the atoms listed above, the ground-state electron density computed with the angularly dependent grid turns out to spherically symmetric and our results for ground-state total energy and KS eigenvalues agree well with those of Ref. 24. Minor differences are due to the fact that in our study, we used an interpolation for the exchange-correlation energy of the electron gas (PZ, see Ref. 29) slightly different from the one (VWN, see Ref. 31) used in Ref. 24. To provide basis functions for the time-dependent simulations, a fairly high number of unoccupied orbitals (up to 162 for P) have been computed for each atom.

As described in Sec. II, the optical properties of atoms are determined by applying a short-time potential and monitoring the time evolution of the electrons well after the external potential returned to zero. In our simplest implementation, the basis for the time evolution under a time-dependent potential is provided by filled and empty KS orbitals computed for the ground-state configuration. In the present testing stage, in particular, the basis includes predominantly, and in a few cases exclusively, empty states related to ground-state occupied orbitals by a dipole transition. In the case of Be, for instance, the ground-state configuration is $1s^2 2s^2$, and only empty states of p_z symmetry are considered. This symmetry-restricted basis is sufficient to describe linear response, but excludes part of the nonlinear contributions. Including all virtual states up to a given cutoff energy would increase somewhat the cost of the computation, but, in most cases of interest, it would remain a task suitable for a desktop PC.

The set of basis functions used for each atom is listed in Table I. For each atom, the eigenvalues of the empty orbitals included in the basis cover an energy span of about 2 Ha, well beyond the energy of the lowest-energy excitation. The error on the frequency of the lowest-energy excitation due to the incomplete basis is estimated at 1 mHa, i.e., comparable to the uncertainty due to the finite duration (48 fs) of our simulations. The convergence of the oscillator strength is somewhat slower, but still within a few percent.

The reason underlying the fairly large basis set required to achieve convergence can be described as follows. As already pointed out several times in the literature, LSD (and simple gradient corrected schemes such as GGA) underestimates the binding of empty KS orbitals, and thus overestimates,

TABLE I. List of atomic orbitals used for the time-dependent simulations of select atoms. The states in the list are available for each spin, unless otherwise stated. M is the total number of orbitals in the basis.

Element	M	Basis			
He	80	$1 \times s$	$40 \times p_z$		
Li	60	$2 \times s^{\uparrow}$	$1 \times s^{\downarrow}$	$30 \times p_z$	
B	80	$2 \times s$	$40 \times p_z$		
N	95	$2 \times s$	$1 \times p_x^{\uparrow}, p_y^{\uparrow}$	$30 \times p_z$	$15 \times d_{zz}, d_{zx}, d_{zy}$
Ne	82	$8 \times s$	$1 \times p_x, p_y$	$13 \times p_z$	$6 \times d_{zz}, d_{zx}, d_{zy}$
Na	67	$6 \times s$	$1 \times p_x, p_y$	$9 \times p_z$	$5 \times d_{zz}, d_{zx}, d_{zy}$
Mg	108	$8 \times s$	$1 \times p_x, p_y$	$21 \times p_z$	$8 \times d_{zz}, d_{zx}, d_{zy}$
P	177	$20 \times s^{\uparrow}$	$11 \times s^{\downarrow}$	$2 \times p_x^{\uparrow}, p_y^{\uparrow}$	$1 \times p_x^{\downarrow}, p_y^{\downarrow}$
		$30 \times p_z$	$18 \times d_{zz}^{\uparrow}, d_{zx}^{\uparrow}, d_{zy}^{\uparrow}$	$9 \times d_{zz}^{\downarrow}, d_{zx}^{\downarrow}, d_{zy}^{\downarrow}$	
Ar	106	$11 \times s$	$4 \times p_x, p_y$	$14 \times p_z$	$8 \times d_{zz}, d_{zx}, d_{zy}$
Ca	92	$10 \times s$	$2 \times p_x, p_y$	$14 \times p_z$	$8 \times d_{zz}, d_{zx}, d_{zy}$
Zn	150	$10 \times s$	$5 \times p_x, p_y$	$19 \times p_z$	$10 \times d_{zz}, d_{zx}, d_{zy}$

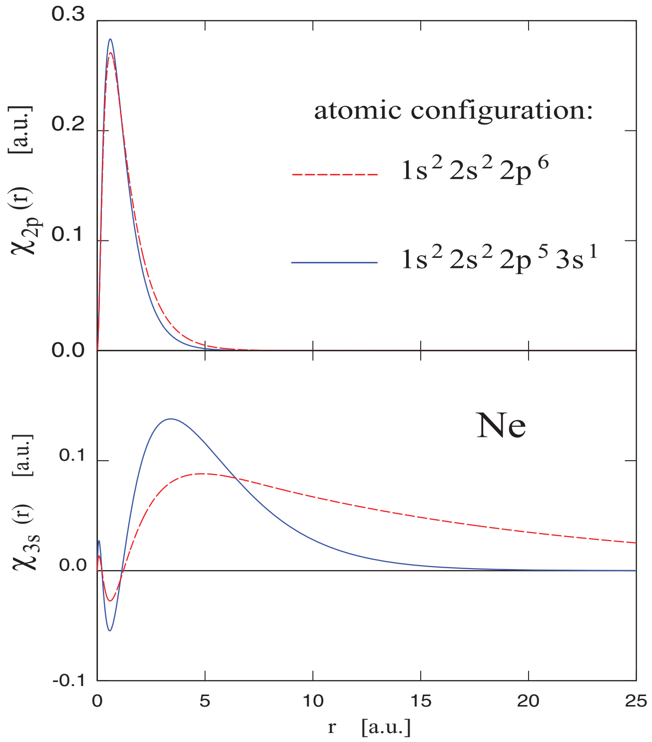

FIG. 2. (Color online) Filled ($2p$) and lowest-energy ($3s$) empty state of Ne. In the notation of Sec. II, $\chi_\nu(r) = r\psi_\nu(r)$.

sometimes drastically, their spatial extension. As a way of example, we show in Fig. 2 the radial plot of the $3s^0$ state of Ne, which extends well beyond the range of the highest occupied ($2p^6$) orbital. The overestimation of the orbital size is particularly apparent if we compare the orbitals in Fig. 2 with their counterparts computed upon promoting one electron from the $2p^6$ to the $3s^1$ state ($1s^2 2s^2 2p^6 \longrightarrow 1s^2 2s^2 2p^5 3s^1$). In the $1s^2 2s^2 2p^6$ configuration, the potential felt by the $3s^0$ orbital is fully screened by the ten electrons in their ground state, while in the $1s^2 2s^2 2p^5 3s^1$ configuration, the excited electron feels an ionic potential of effective charge $Z^* = 1$. This second case is likely to provide a more realistic picture of the potential felt by electrons in an excited state. As a result of the difference in the effective potential, the $3s^1$ orbital is much narrower than the $3s^0$ one.

The overestimation of the spatial extent of empty orbitals by LSD is not always as drastic as the one illustrated for Ne. In the case of Na, for instance, the computation of the $3p$ orbital by the two methods described above for Ne gives similar results. In general, we find that the overestimation of the spatial extent of low lying empty states is particularly important for closed shell atoms. Nevertheless, in all cases, the superposition of many virtual KS orbitals is required to reproduce the precise geometry of the excited states.

These qualitative considerations, already extensively discussed in the literature, will guide us in the interpretation of the time-dependent results and will provide the major motivation for experimenting with a a set of optimally localised basis functions (see Appendix).

During the time evolution, the value of the Kohn-Sham functional evaluated at the instantaneous density provides a first test of the accuracy of the integration scheme. Although $E_{\mathrm{KS}}[\rho(t)]$ cannot be interpreted easily in terms of the physical energy for a time-dependent system, it still provides a constant of motion for the system whenever the external time-dependent potential is switched off. The plot of $E_{\mathrm{KS}}[\rho(t)]$ for Be shown in Fig. 3 displays a sharp variation for $0 \leqslant t \leqslant 10$ a.u. while the field is applied, and is virtually constant afterwards. A detailed analysis on a much expanded energy scale reveals a slight violation of energy conservation, whose amplitude turns out to be proportional to the time step used in the simulation. Such a linear scaling is rather unfavourable, but the prefactor turns out to be very small, and long simulations are feasible at an acceptable computational effort. A crucial clue to identify the origin of this integration error is provided precisely by its linear dependence on the time step. This excludes, in particular, a fault of the basis set (in)-completeness, since this type of error, once gauged on a constant interval of time, would not decrease with decreasing δt. It excludes also round-off effects, since these would increase with decreasing time step. An obvious source of error with the observed linear scaling with δt is represented by the approximate integration required to go from Eq. (20) to Eq. (21). We think that this is indeed the origin of the slight energy nonconservation, and the point to be improved to allow simulations much longer than those carried out in our study.

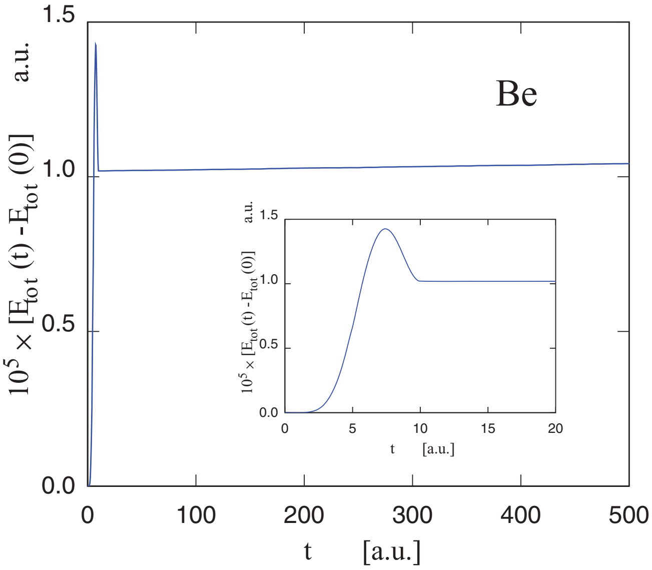

FIG. 3. (Color online) Time dependence of the Kohn-Sham functional E_{KS} evaluated at the instantaneous electron density $\rho(t)$ during the real-time simulation (see text) of a Be atom. The external perturbation is active for $0 \leqslant t \leqslant 10$ a.u.

The result of real-time simulations reveal two qualitatively different pictures that in what follows, are referred to as the normal case, concerning Li, Be, Na, Mg, Ca, and Zn, and the anomalous behavior, observed for He, Ne, N, Ar, and P. We discuss first the results obtained for the normal case.

The dipole moment $P_z(t)$ computed for the Be atom following the application of the external perturbation of Eq. (27) at $t = 0$ is shown in Fig. 4. The dependence of the result from the initial time of the simulation is removed by computing the time-autocorrelation function $A(t)$ of the dipole (see Fig. 5). The oscillations in $A(t)$ apparent in

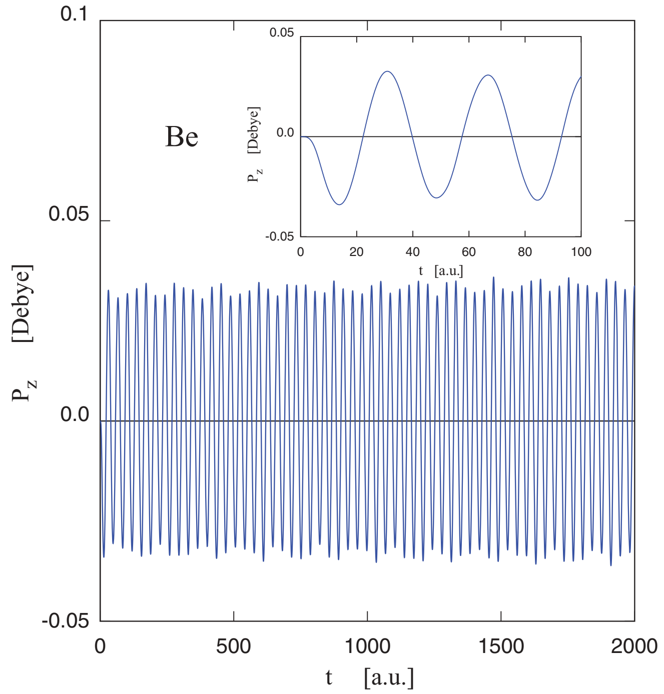

FIG. 4. (Color online) Time dependence of the fluctuating electrostatic dipole moment d_z of a Be atom during and after a short-time perturbation ($0 \leqslant t \leqslant 10$ a.u.) to the atomic ground state (see text).

Fig. 5 persist on a time scale much longer than what we can follow in our simulations. To avoid Fourier transforming a discontinuous function, we multiply $A(t)$ by a linear function $F(t)$, which assumes the value $F = 1$ at $t = 0$ and vanishes at $t = 2000$ a.u., corresponding to the length of our simulations. The effect of this linear scaling is shown in Fig. 5(b). Needless to say, this procedure changes somewhat the size and phase of the Fourier components represented in $A(t)$, but a series of tests have shown that the linear form of $F(t)$ minimizes the distortion of the computed spectrum.

The computed absorption spectrum $S(\omega)$ of Be, which is proportional to the imaginary part $\mathcal{I}[\alpha(\omega)]$ of the Fourier transform of $A(t)$, is shown in Fig. 6. A least square fit of the results with a Lorentzian function

$$S(\omega) = \frac{K}{(\omega - \omega_0)^2 + \delta^2} \tag{33}$$

provides an estimate of the basic parameters (ω_0, K, and δ) characterizing the lowest-energy dipole excitation of Be. The results for the energy $\Omega_{\rm RT} = \hbar\omega_0$ of the fundamental dipole excitation of Be and of several other atoms are reported in Table II. The RT label of $\Omega_{\rm RT}$ indicates that this energy is computed by real-time propagation.

The real part of the Fourier transform of $A(\omega)$, related by a Kramer-Krönig transformation to the imaginary part entering the determination of $S(\omega)$, is shown in the inset of Fig. 6, and displays a clear polelike singularity. The agreement of the frequencies computed in this way for Li, Be, Na, Mg, Ca, and Zn is in line with the results of previous studies.[5]

The picture provided by our simulation for light closed shell atoms such as He, Ne, and Ar, but also for N and P is

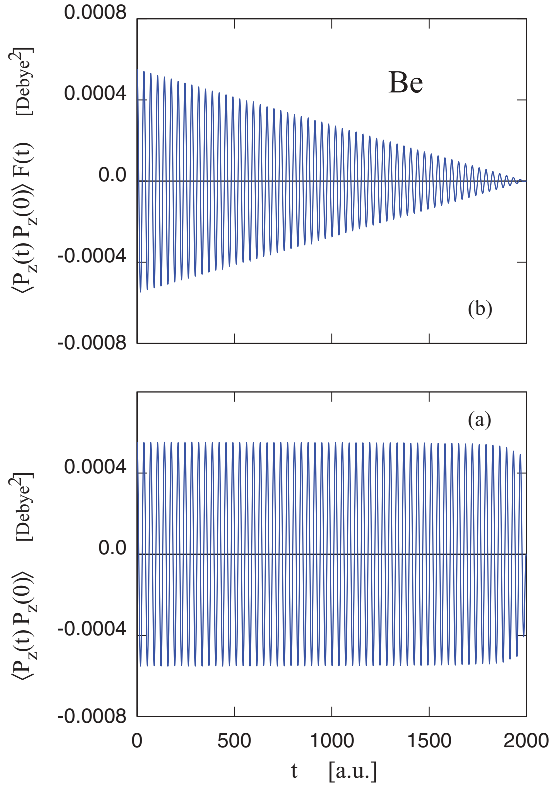

FIG. 5. (Color online) (a) Time autocorrelation function $A(t) = \langle P_z(t) P_z(0)\rangle$ of the fluctuating dipole moment shown in Fig. 4. Real-time simulation of a Be atom with 0.01 a.u. time step. (b) Result of multiplying $A(t)$ times a linear function that vanishes at the upper limit of the simulation time (see text).

qualitatively different from the one discussed above for *normal* transitions. The first indication of a difference between the two cases is provided by the plot of the oscillating dipole, shown in Fig. 7 for Ne. Instead of the nearly sinusoidal oscillation seen in the case of Be, the time-dependence of $P_z(t)$ for Ne displays clear beatings at moderate size of the basis

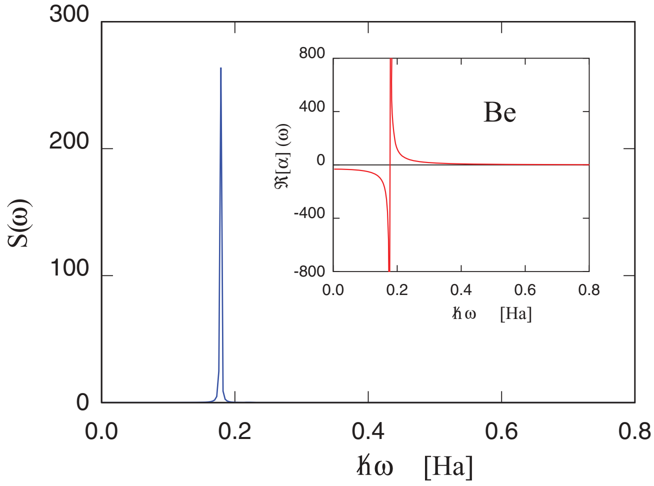

FIG. 6. (Color online) Adsorption spectrum computed from the time autocorrelation function of Fig. 5. Real-time simulation of a Be atom with 0.01 a.u. time step.

TABLE II. Dipole excitation energies (Ha) of neutral atoms. Ω_{exp} is the experimental value,[20] Ω_{RT} is calculated from real-time propagation (this study), Ω_{LR} is the linear-response calculation $\Omega_{\Delta\mathrm{SCF}}$ is the total energy difference, and ω_{ij} is the Kohn-Sham Eigenvalue difference. Quantities in parenthesis are the percentage errors, relative to the experimental values. Linear response calculations: (a) Ref. 8; (b) Ref. 43; (c) Ref. 33; (d) Ref. 44. A star next to ω_{ij} indicates that the eigenvalue of dipole-excited state is positive within LSD. For each transition, the first item in the $\Omega_{\Delta\mathrm{SCF}}$ column has been computed assuming a spherically symmetric ground and excited state, using fractional occupation numbers; the second number, in square brackets, has been computed assuming that the excited electron is promoted to or comes from a p_z state, i.e., the atom is nonspherical following the excitation. For N and P, we list different transitions: (α): $2s^2 2p^3 \longrightarrow 2s^2 2p^2 3s$; ($\beta$): $2s^2 2p^3 \longrightarrow 2s^1 2p^4$; ($\gamma$): $3s^2 3p^3 \longrightarrow 3s^2 3p^2 4s$; and ($\delta$): $3s^2 3p^3 \longrightarrow 3s^1 3p^4$.

	Ω_{exp}	Ω_{RT}	Ω_{LR}	$\Omega_{\Delta\mathrm{SCF}}$	ω_{ij}
He	0.7797	0.6115 (21.6)	0.7538 (5.6) (d)	0.7608 (2.4) [0.7562] (3.0)	0.6105 (21.7)*
Li	0.06791	0.07213 (6.2)	0.0745 (9.7) (b)	0.06729 (0.9) [0.06143] (9.5)	0.06742 (0.7)
Be	0.1939	0.1784 (8.0)	0.1995 (2.9) (a, b) 0.1772 (8.6) (c)	0.1283 (33.8) [0.1225] (36.8)	0.1286 (33.7)
N	0.3799 (α)	0.2977 (21.6)	0.3156 (16.9) (d)	0.4391 (15.6) [0.4425] (16.5)	0.3410 (10.2)*
	0.4019 (β)			0.3991 (0.7) [0.3913] (2.6)	0.4010 (0.2)
Ne	0.6126	0.4936 (19.4)	0.496 (19.0) (b) 0.5418 (11.6) (d)	0.6285 (2.6) [0.6358] (3.8)	0.5005 (18.3)*
Na	0.07259	0.08258 (13.8)	0.08213 (13.1) (d)	0.08120 (11.9) [0.07565] (4.2)	0.08010 (10.3)
Mg	0.1597	0.1556 (2.6)	0.1755 (9.9) (a, b)	0.1266 (20.7) [0.1224] (23.4)	0.1250 (21.7)
P	0.2552 (γ)	0.2133 (16.4)	0.2175 (14.8) (d)	0.2505 (1.8) [0.2539] (0.5)	0.2186 (14.3)*
	0.2717 (δ)			0.2991 (10.1) [0.2959] (8.9)	0.2995 (10.3)
Ar	0.4249	0.3653 (14.0)	0.3899 (8.2) (d)	0.4275 (0.6) [0.4348] (2.3)	0.3758 (11.6)*
Ca	0.1078	0.1132 (5.0)	0.1315 (22.0) (a, b)	0.08921 (17.2) [0.08630] (19.9)	0.08846 (17.9)
Zn	0.2130	0.2086 (2.1)	0.2385 (12.0) (a, b)	0.1800 (15.5) [0.1775] (16.7)	0.1761 (17.3)

(34 orbitals), turning into a chaotic behavior when the simulation is carried out at full convergence with a large number (82 orbitals) of basis functions. This difference is reflected in the behavior of the time autocorrelation function of the fluctuating dipole, shown in Fig. 8. The dipole adsorption spectrum of Ne and of the other atoms of the same class consists of a series of regularly spaced lines, whose envelop identifies a very broad line shape covering the energy range in which the true excitation energy is expected and measured in experiments (see Fig. 9).

The distinction between normal and anomalous cases, as well as the broadening of sharp lines into a discrete but relatively dense band has already been observed in the past[9] and attributed to the upward shift of the LSD KS potential with respect to the exact one.[32] Normal cases, then, correspond to atoms whose lowest-energy dipole-excited state is still bound, despite the LSD error. Anomalous cases, instead, correspond to atoms whose lowest-energy dipole-excited state is raised into the continuum, giving origin to a resonant state. The residual discretization of the spectrum of anomalous atoms is due, in our computations, to the finite volume of the sphere enclosing the simulated atoms.

Another, more relevant manifestation of the same effect is the sensitivity of the simulation result on R_{max}. While the spectra of normal atoms converges fairly quickly with the box size, convergence is slow in the case of anomalous atoms, because of the delocalized character of their excited states. This is illustrated in Fig. 10, showing the absorption spectrum of helium, which is the prototypical anomalous case. The significantly different frequencies seen at different R_{max} values correspond to excitations from the $1s$ state to extended states of p_z symmetry, having their first radial node at R_{max}. This interpretation is confirmed by plots of the charge variation due to the excitation as a function of time.

In the case of anomalous atoms and for all R_{max} considered in our simulations, the frequency of the lowest-energy excitation is significantly below the experimental absorption energy and lower than previous computational estimates by TD-DFT-ALDA. This last discrepancy is due to the sensitivity of the result on the basis set used in the computation. In most cases, previous computations used a discrete basis of Gaussian or Slater functions, excluding *a priori* the extended states that in our computations on a logarithmic mesh provide the lowest-energy transitions. The significant underestimation

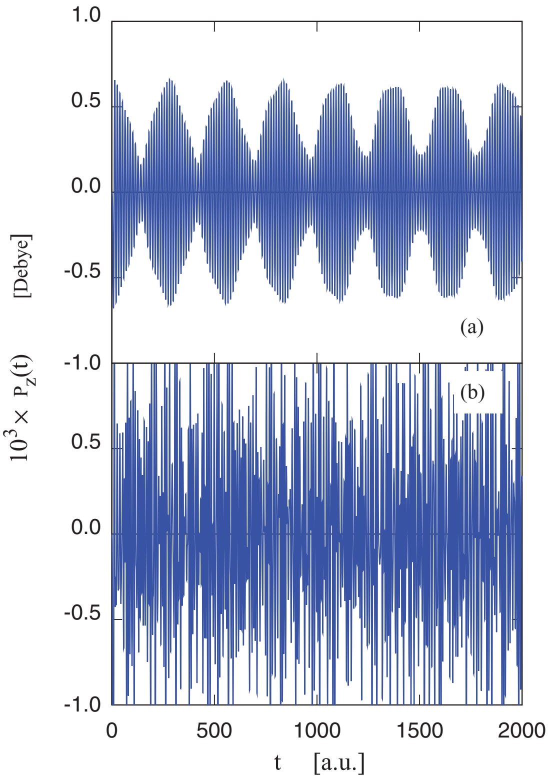

FIG. 7. (Color online) Time dependence of the fluctuating electrostatic dipole moment d_z of a Ne atom during and after a short-time perturbation ($0 \leqslant t \leqslant 10$ a.u.) to the atomic ground state. Basis set consisting of (a) 34 and (b) 82 orbitals.

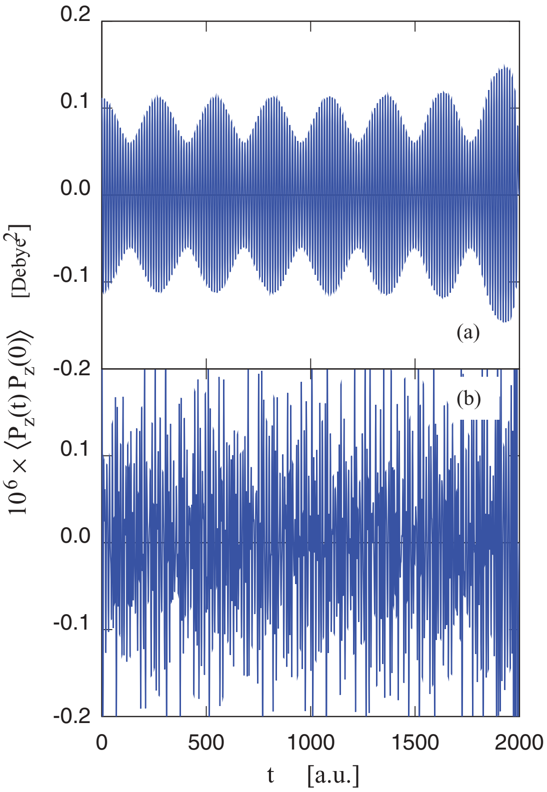

FIG. 8. (Color online) Time autocorrelation function $A(t) = \langle P_z(t)P_z(0)\rangle$ of the fluctuating dipole moment of Ne. Basis set consisting of (a) 34 and (b) 82 orbitals.

of TD-DFT-ALDA excitation energies of anomalous atoms with respect to the corresponding experimental data is due to the fact that the lowest-energy transition found by simulation connects the ground state to continuum states of approximately zero energy. In experiments, such a transition to an unbound state requires higher energy, above the threshold for the dipole transition to the lowest-energy bound state of appropriate symmetry. This problem is less apparent and less relevant for molecules, whose lowest excitation energies are never as large as those of closed shell atoms. This observation emphasizes the role of atoms as sensitive test cases for TD-DFT approximations.

Remarkably, in He and in all other anomalous atoms, one excitation line found by simulation is fairly insensitive to changes in $R_{\rm max}$, and its frequency is close to both the experimental value, and to previous estimates using the linear response approach, on a basis of localized functions. This observation could be explained easily in terms of the resonance nature of the genuine excited states, and, in principle, could provide a way to extract the relevant information from simulation data. However, we do not emphasize this point here, because distinguishing the physical transition from the spurious ones remains a difficult and time consuming task, requiring multiple simulations with different $R_{\rm max}$ values.

Again in the case of the closed-shell atoms He, Ne, and Ar, we observe that the lowest energy line computed by TD-DFT hardly differs from the corresponding difference of KS eigenvalues. This is easily understood on the basis of the linear response route to TD-DFT energies. Let us consider the transition from a state i of orbital $\phi_i(\mathbf{r})$ to state j of orbital $\phi_j(\mathbf{r})$. According to Ref. [8], and assuming that the $i \longrightarrow j$ transition is unaffected by any other dipole-allowed excitation, the TD-DFT correction to the eigenvalues difference ω_{ij} is

$$\Delta\omega_{ij} = \iint \phi_i(\mathbf{r})\phi_j^*(\mathbf{r})\left[\frac{1}{|\mathbf{r}-\mathbf{r}'|} + f_{\rm xc}(\mathbf{r},\mathbf{r}')\right] \times \phi_i^*(\mathbf{r}')\phi_j(\mathbf{r}')d\mathbf{r}d\mathbf{r}', \qquad (34)$$

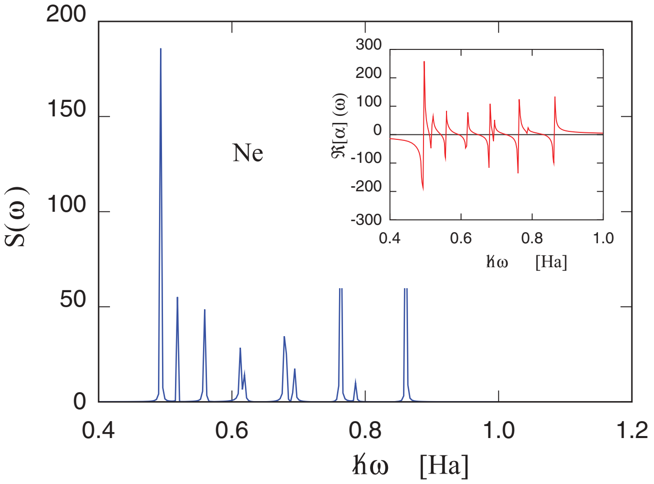

FIG. 9. (Color online) Dipole absorption spectrum computed for Ne. Real-time simulation with 0.01 a.u. time step.

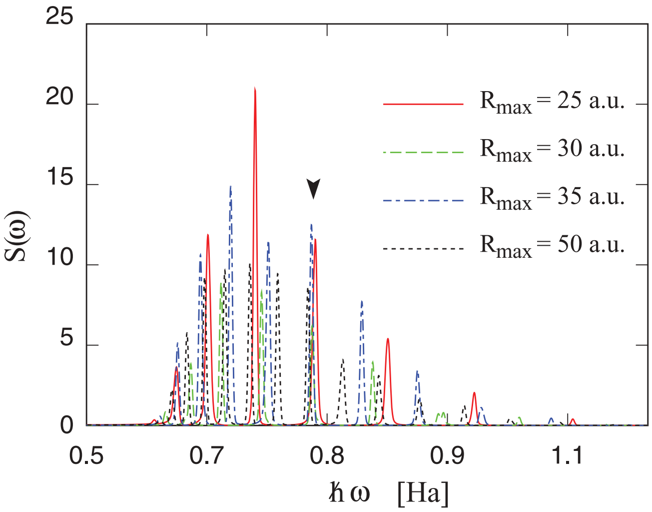

FIG. 10. (Color online) Dipole absorption spectrum of helium, computed using different values of the simulation box size R_{max}. The vertical arrow at $\hbar\omega = 0.7844$ Ha closely matches previous computational estimates using the linear response formulation as well as the experimental excitation energy at 0.7797 Ha.

where f_{xc} is the exchange-correlation kernel and a static (adiabatic) approximation is implied. Then, it is easy to verify that such a correction has to vanish in the case that the transition connects a localised bound state i to a delocalized scattering state j.

The TD-DFT correction to the eigenvalues difference is more sizable in the case of normal atoms, and, as expected, TD-DFT excitation energies tend to be closer to the experimental value than the estimate based simply on ω_{ij}. It might be useful to note, however, that there are exceptions to this rule, such as Li and Na (see Table II), for which the ω_{ij} estimate is in better agreement with experiments than the TD-DFT result. Again, in the case of the normal atoms, the results of our real-space real-time simulations are close to those obtained using the linear response formulation of TD-DFT. Differences are likely to be due primarily to computational reasons such as the different basis used by us and by previous computations. Another reason could be related to the different account of spin multiplicities in the linear response computation and in our real-space real-time approach. This point will be briefly commented on in the conclusive section. Because of the symmetry change, the dipole excitation energy for the atoms listed in Table II can be computed also as a total energy difference (ΔSCF) between the ground- and excited-state configuration. The results are much better than the TD-DFT ones in the case of the anomalous atoms. The performance for the normal cases is rather mixed, alternating good results for Li and Na, to apparent failures of the ΔSCF approach for Be, Mg, Ca, and Zn. The total energy difference route suffers from the additional complications that assuming a spherically symmetric or a broken symmetry excited states gives different results for the excitation energy. Once again, the change in spin multiplicity upon excitation could also slightly affect the result.

It might be worth emphasizing once again that the distinction between normal and anomalous behavior is strictly dependent on the approximation for the exchange and correlation potential, and the anomalous behavior is, in all cases, an artifact of the LSD-ALDA model, since even closed-shell atoms in reality have an infinite number of excited bound states, asymptotically giving rise to a series of Rydberg states. Slightly different XC approximations such as GGA's are not expected to overcome the LSD problem, since their exchange-correlation potential still suffers from the major limitations of the LSD potential, and their KS spectra are nearly indistinguishable from those of LSD. Hybrid functionals such as B3LYP[35] or PBE0,[36] incorporating part of the exact exchange, perform somewhat better in this respect, but still significantly underestimate the long-range attractive tail of the KS potential. More refined functionals, whose potential reflects the correct asymptotic $-1/r$ form, are required to cure this problem. This is confirmed by the results of Ref. 33 and 34, showing that an approach computing the ALDA linear response upon evolving the electron density within the exact KS potential provides excellent excitation energies for He and Ne. Similar results have been obtained by other authors[8,16,17] using the optimized effective potential[37] and/or the self-interaction corrected approximation[29] to compute the ground-state potential and the exchange-correlation kernel. To illustrate this point and to emphasize the crucial role of the exchange-correlation functional in the discrimination of normal and anomalous atoms, we carried out additional simulations for He within the exact-exchange approximation (EXX), using Hartree Fock exchange and no correlation. The usage of EXX turns the anomalous response of He into a regular one, as could be seen in Fig. 11, comparing the time autocorrelation function of the P_z dipole of He computed within LSD and within EXX. The Fourier transform of the EXX time autocorrelation function now gives a spectrum consisting (almost) of a single line, whose energy $\Omega_{\mathrm{RT}} = 0.7970$ Ha is in fair agreement with the experimental value $\Omega_{\mathrm{exp}} = 0.7797$ Ha.

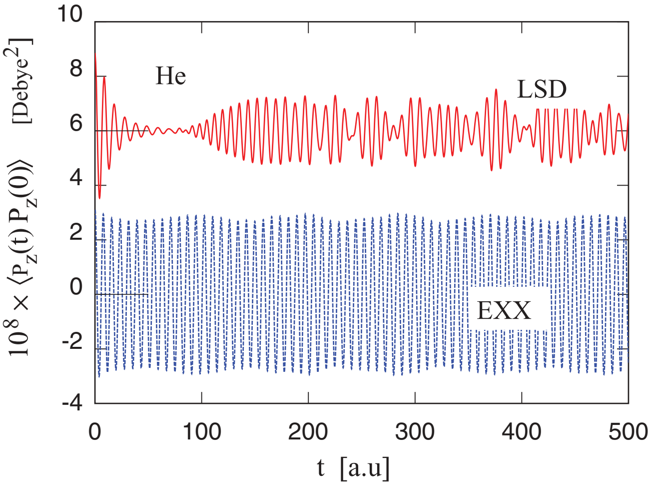

FIG. 11. (Color online) Comparison of the time autocorrelation function $A(t) = \langle P_z(t)P_z(0)\rangle$ of He computed by the local spin density approximation (LSD, full line, red) and by the exact exchange approximation (EXX, dotted line, blue). For the sake of clarity, the LSD result has been moved vertically by a constant shift of six units.

IV. TD-DFT SIMULATION OF AUGER PROCESSES

The good performance of TD-DFT in predicting the optical absorption spectrum of *normal* atoms, and the realization that the problematic results for the *anomalous* atoms may be traced back to ALDA, should not conceal the fact that other fundamental problems might be hidden in the TD-DFT formulation. An indication that something important is missing in the present theory is provided by the results of a simple simulation meant to reproduce an Auger process.[38]

The Auger de-excitation mechanism may be activated whenever a high-energy electromagnetic perturbation such as an x or γ ray removes a core electron from an atom. Then, the excited state may decay by filling the low-lying hole with an electron from the higher energy levels. Energy conservation implies that a photon is emitted during this process, whose energy (E_{eh}) is discretized by the energy quantization of the hole and of the the electron giving rise to the process. Before leaving the atom, the photon might further ionize the A^+ atom into A^{2+} by stripping an electron from the valence states. Under normal conditions, this process competes with other relaxation channels. The signature of a genuine Auger process is the monochromatic character of the emitted electron, whose kinetic energy corresponds exactly to the E_{eh} energy of the virtual photon, minus the (usually negligible) binding energy of the valence electron.

Our all-electron implementation of TD-DFT allows us to simulate this process by a computational experiment in which, starting from an atomic ground state, we remove an electron from a core level. An almost ideal experimental realization of the computational process might be represented by the so-called positron annihilation Auger electron spectroscopy (PAES)[39] in which a fairly low-energy ($\sim$10 eV) positron penetrates into the core region and annihilates one core electron, without perturbing significantly the atom prior to the sudden event.

The TD-DFT simulation of the atom following this drastic excitation shows a fast collective reorganization of the electron cloud that soon results in the outwards propagation of one or, usually, more electrons. A suitable absorbing potential, continuously removing charge from the outer portion ($r \geqslant 25$ a.u.) of the simulation cell, is introduced to approach the open boundary condition of real experiments.

Figure 12 displays the time evolution of the total charge in the system upon removing a 1*s* (a) or a 2*s* (b) core electron from Mg. As can be seen in the figure, the charge decreases smoothly with time, and the simulation results are strongly suggestive of a thermal evaporation process progressively taking place in the highly excited atom. A different visual representation of the same process is given in Fig. 13. Even though the electron density is still spherically symmetric upon removing a 1*s* or 2*s* electron, it is apparent that symmetry is rapidly broken during the time evolution of the excited atom. The thermal relaxation channel illustrated by these figures is certainly one of the competing de-excitation modes available to the excited atom, but it is nevertheless apparent that the simulation results differ by several important features from the known experimental picture.

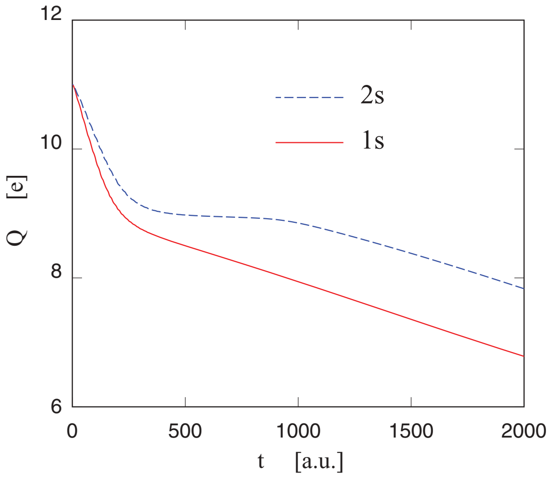

FIG. 12. (Color online) Electronic charge on the Mg atom as a function of time following the sudden annihilation at $t = 0$ of one electron in the 1*s* (full line) and in the 2*s* (dash line) orbitals.

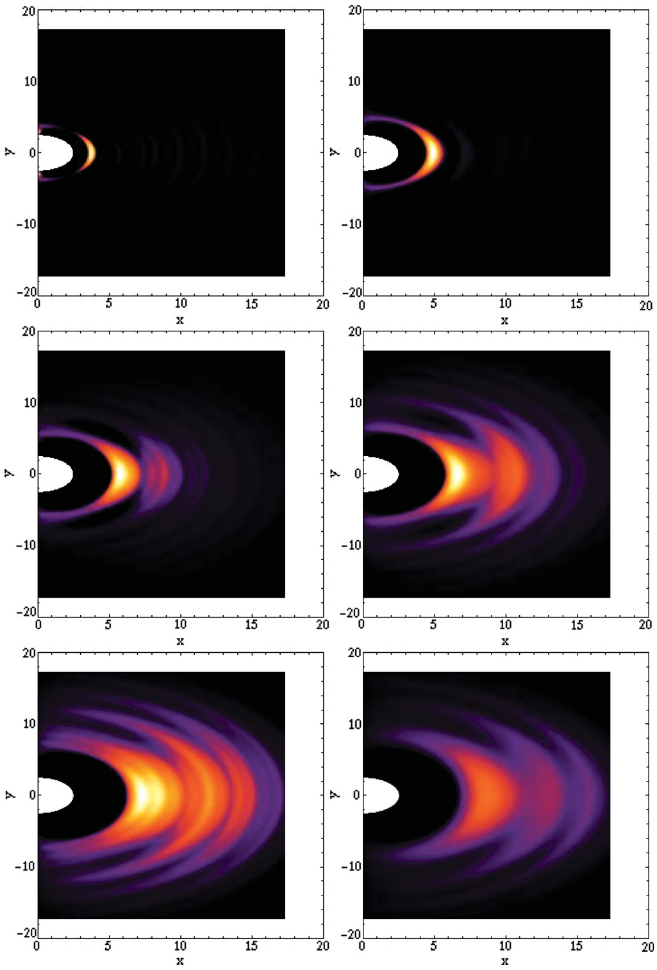

FIG. 13. (Color online) Deviation $\Delta\rho_e(x,y,z=0,t)$ of the time-dependent electron density $\rho_e(x,y,z=0,t)$ from the ground-state density of a Mg atom, following the sudden removal of a 1*s* electron. $\Delta\rho_e(x,y,z=0,t) = \rho_e(x,y,z=0,t) - \rho_e(x,y,z=0,t=0)$. From top to bottom and from left to right, the panels correspond to $t = 5$, 10, 15, 20, 25, and 30 a.u. Magenta, red, and yellow regions correspond to excess charge of increasing size. The white hole at the center represents a large charge deficit.

First of all, no discontinuity is observed when crossing an integer value of the residual (or emitted) charge. In other words, and not surprisingly, there is no sign of the particle nature of electrons, and the final result after all the dust is settled, is likely (in fact certain) to correspond to an ion of fractional charge. The result might be interpreted in terms of the superposition of different ionization states, but this might be a rather arbitrary interpretation, not firmly grounded on a rigorous TD-DFT formulation.

Moreover, and perhaps more importantly, there is no sign of a genuine Auger process. Electrons already leave the atom with just enough energy to overcome the barrier separating the inner atomic region from the outer simulation range. This is markedly different from the Auger picture in which electrons are emitted at a well defined energy, leaving behind an ion whose electrons are in their lowest-energy state.

Needless to say, the purely electromagnetic relaxation channel in which a high-energy photon carries away all of the excitation energy, transferring it to only one of the valence electrons, is completely missing from the simulation picture, and it could not conceivably be described by a scheme that does not quantize the oscillations of the electromagnetic field.

These observations, which, of course, do not affect the value of TD-DFT as an effective computational tool able to predict a significant portion of optical experiments, still point to fundamental limitations of the TD-DFT formulation, apparently related to an incomplete incorporation of basic quantum-mechanical principles into the present theory.

V. SUMMARY AND CONCLUSIONS

Ground-state properties and dipole excitation energies for atoms with up to 30 electrons have been computed by a DFT approach, using a 3D mesh consisting of N_Ω rays emanating from the nucleus. The rays' directions have been selected according to the rules of Ref. 30, allowing the integration of angular variable to be carried out via a Gauss formula. On each ray, orbitals are represented on a logarithmic radial mesh. In our computations, $N_\Omega = 32$, and the integration rule allows us to integrate exactly spherical harmonics components up to $l = 9$. Atoms are enclosed in a sphere of finite radius R_{max}, and thus the spectrum is discretized both at negative and positive energies. The logarithmic mesh consists of 2000 grid points, allowing accurate computations at the all-electron level.

The results of ground-state atomic computations carried out in the LSD approximation agree well with those of previous studies.[24] Moreover, these tests confirm the computational stability and efficiency of the scheme. As a result, a large number of occupied and empty KS orbitals can be computed on the combined angular-radial grid, at a very modest computational cost.

The purpose of our scheme, however, is to carry out real-time real-space simulation of the atoms' evolution under a perturbing external field, breaking the spherical symmetry of the ground state. To test the ability of our approach to carry out such a task, we implemented a TD-DFT-ALDA simulation scheme, evolving states on a discrete basis of M orthonormal orbitals, each represented on the same logarithmic-radial and angular mesh described above. Starting from the atomic ground state, the system is perturbed by the application of an external, time-dependent field of the appropriate angular symmetry. The response of the system is analyzed after the external field is switched off, and quantified by computing time autocorrelation functions of the induced multipolar charge oscillations, whose Fourier transform provides the absorption spectrum in the energy representation.

At each time step, the instantaneous KS Hamiltonian matrix (of $M \times M$ dimensions) is diagonalized, then the matrix representing the time evolution operator is computed and transformed back to the original basis. The size M required to reach convergence depends on the energy interval that needs to be covered, and, to some extent, on the details of the spectrum of the atom under consideration. For all the atoms that we considered, a basis of less than 200 basis functions has been sufficient to converge the estimate of the fundamental dipole excitation energy to within $\sim 10^{-3}$ Ha. This value of M corresponds to a fully manageable computational task, requiring about one day of CPU time on a desktop or laptop computer to follow the time evolution of atoms with 20–30 electrons over approximatively 50 fs.

The reliability of the time evolution is confirmed by the excellent conservation of energy during the long simulation time following the switch-off of the time-dependent external potential. We verified that the amplitude of the energy nonconservation depends linearly with the size of the time step. At the $\delta t = 0.01$ a.u. of our simulations, the violation of the energy conservation over 48 fs is of the order of the μHa.

The focus of the present work has been on the computational part of the problem. Nevertheless, we think that our results for the excitation energies, obtained by a method whose convergence can be easily checked and systematically improved, could provide a useful benchmark to gauge other computational approaches.

In agreement with previous discussions of TD-DFT-ALDA computations for atoms,[9] we observe two qualitatively different patterns in the response of atoms perturbed by a dipolar field. In the first case, that we termed *normal* and is exemplified by Li, Be, Na, Mg, Ca, and Zn, the dipole oscillations display a highly predominant frequency, corresponding to the transition from the ground state to a bound first excited state. Convergence in the number of basis functions and in the size R_{max} of the simulation box occurs fairly quickly.

In the second case, that we termed *anomalous* and is exemplified by He, Ne, N, Ar, and P, we observe several different frequencies, connecting the ground state to unbound excited states, corresponding to a discretized version of the continuum spectrum of an isolated atom in vacuum. The result converges relatively poorly with the basis set size and is sensitive to the size of the simulation box.

In general, we observe that the TD-DFT-ALDA prediction of the excitation energy of atoms is somewhat better, but not systematically so, than the estimate based on the KS eigenvalue. Of course, the TD-DFT estimate is on a sound conceptual ground, while the interpretation of eigenvalues as orbital energies is not justified.[40] In all cases, however, it is apparent that the ability of simple approximations such as LSD-ALDA to predict dipole excitation energies of atoms is relatively poor, partly contradicting the popular opinion that this approach is generally good for finite systems. This state of affairs is particularly surprising and disappointing, given the basic nature of dipole optical transitions in atoms and given the abundance of highly accurate experimental data.[20] More rigorous many-body methods such as GW supplemented by the Bethe-Salpeter approach seem to be more successful,[41] but, even in this case, further computations are needed to fully assess the quality and reliability of these methods for atoms.

It might be useful to point out that the quality of the TD-DFT-ALDA results is particularly poor for the anomalous atoms, since, in this case, the lowest frequency given by simulation (and also by the linear approximation) corresponds to the transition to the lowest unbound state, whose energy (approximately zero) falls below that of the genuine excited state, which appears as a resonance in the continuum of unbound states.

These observations, reflecting and confirming the picture already available in the literature, emphasize the need of approximations for the static and time-dependent exchange-correlation functionals to go beyond the simple LSD and ALDA levels. This conclusion is supplemented and strengthened by the results of a further series of simulations, mimicking an Auger process initiated by removing a core electron. The results show a multitude of thermal relaxation processes in which electron progressively evaporate from the atom, leaving it in a rather unphysical state of partial charge. While some justification of this result could be found in terms of a statistical or ensemble description of the relaxation and ionization process, it is nevertheless clear that the genuine Auger process is missing from the simulation picture. The primary reason for this failure is the apparent lack of quantization of the electromagnetic field.

We point out that, following the practice established by previous real-space real-time TD-DFT simulations, in our study, we neglected the problem of spin multiplicities and spin contamination, which, instead, has to be considered for a more quantitative comparison with experiments and with TD-DFT computations based on the linear response formulation, which often correctly include these aspects. Attempts to describe spin multiplicity and remove spin contamination in real-time real-space computations have been reported,[42] but, in this respect, the simulation route appears to be less straightforward than the linear response one.

As a last remark, we observe that the efficiency of TD-DFT computations can be improved by resorting to a physically motivated basis for the excited states (see Appendix below), that consists of ground-state orbitals and of their derivatives with respect to a perturbation. Several tests have shown that the precise form of the perturbation is not crucial to produce a suitable basis set. However, in our computations, response basis functions have been generated by considering the derivatives of orbitals with respect to static dipole perturbations. The results for simple atoms, involving only the excitation of s electrons, display a remarkably quick convergence of the results as a function of the basis set size. The reason of the improvement is the enhanced localization of response functions with respect to empty KS orbitals, which, feeling only a fully screened KS potential, turn out to be far too extended. Moreover, by limiting the size of the functional space available for excitations, a basis of a few response functions can partly compensate the spread of unbound excited states, improving the identification of the genuine fundamental frequency. Linear response methods[7,8,43,44] achieve a similar effect by using a basis set of localized functions, and by setting the number of interacting poles (often a single one) included in the solution of the eigenvalue equations for the excitation energies and oscillator strength.

Response functions had already been introduced in previous studies.[26,27] However, in this paper, the performance of response functions is discussed in detail for time-dependent simulations.

ACKNOWLEDGMENTS

We thank Leonardo Bernasconi for useful discussions and for computing excitation energies of atoms using the linear response formulation of TD-DFT, on a basis of Gaussian functions. We thank Fabio Trani for useful discussions on the role of spin in dipole excitations of atoms. One of us (P.B.) thanks the School of Physics, Trinity College, Dublin, the School of Physics and the Complex and Adaptive Systems Laboratory (CASL), University College Dublin, for their kind hospitality during the last stages of this work.

APPENDIX: RESPONSE BASIS FUNCTIONS

The efficiency of the real-space representation for the KS orbitals contrasts somewhat with the slow convergence of the computed results with increasing size of the basis set. This problem is particularly apparent for the closed-shell atoms manifesting ionizing resonances in their spectra, while for normal cases, the rate of convergence is acceptable, even though the margin for improvement is apparent. In the case of He or Ne, for instance, the amplitude of the induced dipole increases only slowly with increasing basis set size, and a large number of virtual orbitals is required before convergence is really achieved.

The first reason for the slow convergence of the computed response is the exaggerated delocalization of the unoccupied states, while the analysis of fully converged simulations shows that sizable changes in the KS orbitals and in the density take place only in a rather limited region of space, in all cases smaller than the volume covered by empty KS orbitals. As a consequence, the superposition of a relatively large number of virtual states is required to reproduce the localization of the dipole response. These considerations motivated us to search for a basis of optimally localized functions, approaching quickly the fully converged limit and thus reducing drastically the computational time.

In our investigation, we have been guided by the approach and results of Refs. 26 and 27, where the so-called *response* basis set was developed and tested for ground-state computations. The original approach supplements the occupied orbitals with a set of functions representing the derivative of the occupied orbitals with respect to spherical perturbations. Thus, for instance, the successive differentiation of a nodeless orbital of s symmetry gives a sequence of response s functions with one, two, . . . ,n radial nodes, and a similar result holds for all other $l > 0$ orbitals.

Standard perturbation theory tells us that all functions obtained in this way are orthogonal to the occupied states, since

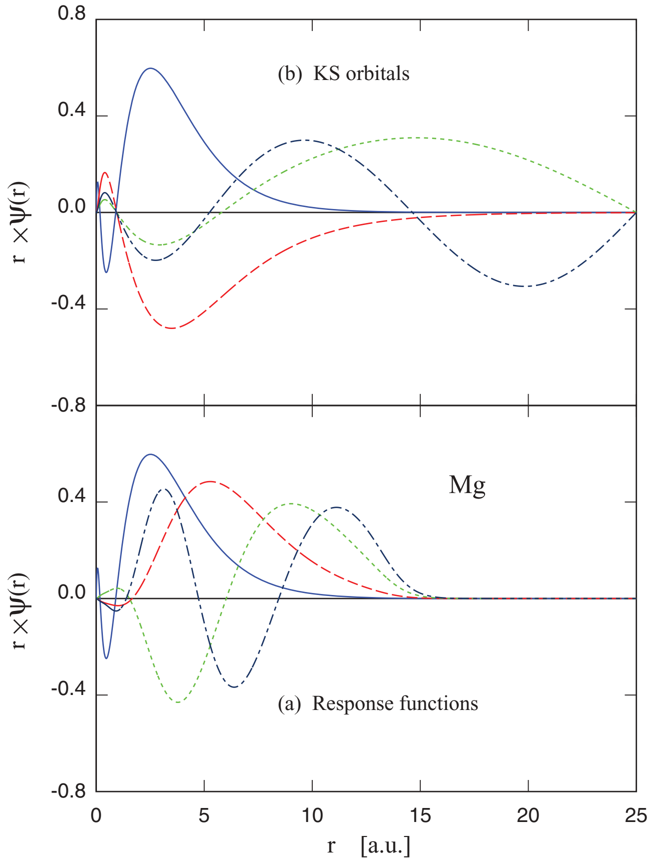

FIG. 14. (Color online) (a) Response functions for the $3s^2$ orbital of Mg. Full line: $3s$ ground-state KS orbital; dash line: first derivative of the $3s$ orbital; dotted line: second derivative of the $3s$ orbital; and dash-dotted line: third derivative of the $3s$ orbital. (b) Filled and empty KS orbitals of Mg. Full line: $3s$ ground-state KS orbital; dash line: $3p$ KS orbital; dotted line: $4p$ KS orbital; and dash-dotted line: $5p$ KS orbital.

they belong to the functions' space spanned by virtual orbitals. Moreover, they can be made orthogonal among themselves, and normalized, by a Gram-Schmidt procedure.

We extend the response basis set approach to the time-dependent case by considering the derivative of occupied orbitals with respect to *static* dipolar perturbations, represented by an electric field oriented along the z direction, of intensity E_z. We emphasise that this is at variance from the original scheme, which was limited to spherically symmetric perturbations. In both cases, it is assumed that upon applying the perturbation, the change of each orbital can be expresses by the Taylor series:

$$\psi_i(\mathbf{r}|E_z) = \psi_i(\mathbf{r}|0) + E_z \frac{\partial \psi_i(\mathbf{r}|0)}{\partial E_z} + \frac{1}{2} E_z^2 \frac{\partial^2 \psi_i(\mathbf{r}|0)}{\partial E_z^2} + O\left(E_z^3\right). \tag{A1}$$

Then, the derivatives $\{\partial \psi_i(\mathbf{r}|0)/\partial E_z\}$, $\{\partial^2 \psi_i(\mathbf{r}|0)/\partial E_z^2\}, \ldots,$ together with the occupied orbitals, are the ingredients required to build the response basis set.

In practice, the first and successive derivatives of each occupied KS orbital are computed numerically upon applying a dipolar external field E_z of increasing strength along the z direction. A simple analysis shows that, to first order, from an s orbital we obtain functions of p_z symmetry, from a p orbitals, we obtain a combination of s and d functions, etc. This analysis is readily extended to higher-order derivatives.

In practice, low-order finite difference expressions for the derivatives are applied, and the results are filtered to remove spurious angular components, and, possibly, high-frequency oscillations in the radial direction. Manipulation of different angular momenta components of orbital derivatives is simplified by representing and storing them on the full $N_r \times N_\Omega$ grid. In a second stage, each response basis function is constructed in such a way to contain only one Y_{lm} contribution. Derivatives containing more than one angular component, such as those of $l > 0$ orbitals, are split into distinct basis functions (of s and d angular character, in the example of the p orbital derivative).

For the sake of simplicity, we consider here excitations of s electrons only, thus avoiding the minor complication represented by response functions arising from different l components of the same orbital derivative with respect to E_z. The results of the basis function generation for the $3s^2$ state of Mg are illustrated in Fig. 14, where the three lowest-order response functions are compared with the virtual states of Mg having the same p_z symmetry and the same number of radial nodes. The enhanced localization of response functions with respect to virtual orbitals is apparent.

The results of computations for the dipole absorption spectrum of selected atoms are collected in Table III. The excitation energies of Na and Mg have been computed keeping fixed the $1s$, $2s$, and $2p$ orbitals, and evolving only the $3s$ states. The results highlight the fast convergence of the computed energies with the (small) size of the basis set.

Needless to say, the choice of the basis does not solve the problems due to the ALDA exchange correlation potential, even though the physically motivated shape and size of the response functions allows us to obtain a quick estimate for the center of mass of the excitation spectrum from computations using just a single response function.

TABLE III. Response function calculation. Magnesium and sodium atoms have been modelled within the fixed core approximation. At order 1, 2, and 3, the basis includes the first, second, and third derivative, respectively, of the highest energy s state with respect to an external E_z field. The percentage error in parenthesis is computed with respect to the benchmark excitation energy computed with the basis of Table I.

	Benchmark	Order 1	Order 2	Order 3
Li	0.07213	0.09499 (31.7)	0.07894 (8.6)	0.07431 (3.0)
Be	0.1784	0.2085 (16.9)	0.1921 (7.7)	0.1796 (0.7)
Na	0.08258	0.09458 (14.5)	0.08718 (5.6)	0.08304 (0.6)
Mg	0.1556	0.1709 (9.8)	0.1643 (5.6)	0.1563 (0.4)

[1] *Frontiers of Optical Spectroscopy*, edited by B. DiBartolo and O. Forte (Springer, Amsterdam, 2005).

[2] E. Runge and E. K. U. Gross, Phys. Rev. Lett. **52**, 997 (1984).

[3] C. A. Ullrich, *Time-Dependent Density-Functional Theory* (Oxford University Press, Oxford, 2010).

[4] K. Burke, J. Werschnik, and E. K. U. Gross, J. Chem. Phys. **123**, 062206 (2005).

[5] G. Onida, L. Reining, and A. Rubio, Rev. Mod. Phys. **74**, 601 (2002); S. Botti, A. Schindlmayr, R. Del Sole, and L. Reining, Rep. Prog. Phys. **70**, 357 (2007).

[6] F. Sottile, F. Bruneval, A. G. Marinopoulos, L. K. Dash, S. Botti, V. Olevano, N. Vast, A. Rubio, and L. Reining, Int. J. Quantum Chem. **102**, 684 (2003). See also: F. Sottile, Ph.D. thesis, Ecole Polytechnique, Palaiseau, France, 2003.

[7] M. E. Casida, in *Recent Advances in Density-Functional Methods*, edited by D. P. Chong (World Scientific, Singapore, 1995), p. 155.

[8] M. Petersilka, U. J. Gossmann, and E. K. U. Gross, Phys. Rev. Lett. **76**, 1212 (1996).

[9] P. Elliott, F. Furche, and K. Burke, in *Reviews in Computational Chemistry*, edited by K. B. Lipkowitz and T. R. Cundari (Wiley, New York, 2009), Vol. 26, p. 91.

[10] K. Yabana and G. F. Bertsch, Phys. Rev. B **54**, 4484 (1996).

[11] M. A. L. Marques, A. Castro, G. F. Bertsch, and A. Rubio, Comput. Phys. Commun. **151**, 60 (2003).

[12] S. Meng and E. Kaxiras, J. Chem. Phys. **129**, 054110 (2008).

[13] T. L. Beck, Rev. Mod. Phys. **72**, 1041 (2000); J. R. Chelikowsky, L. Kronin, and I. Vasiliev, J. Phys.: Condens. Matter **15**, R1517 (2003).

[14] T. A. Arias, Rev. Mod. Phys. **71**, 267 (1999).

[15] S. Goedecker, *Wavelets and Their Application for the Solution of Partial Differential Equations in Physics* (Presses Polytechniques et Universitaires Romandes, Lausanne, 1998).

[16] S.-I. Chu, J. Chem. Phys. **123**, 062207 (2005).

[17] X.-M. Tong and Shih-I Chu, Phys. Rev. A **57**, 452 (1998).

[18] S. S. Leang, F. Zehariev, and M. S. Gordon, J. Chem. Phys. **136**, 104101 (2012).

[19] M. van Fassen, Int. J. Mod. Phys. B **20**, 3419 (2006).

[20] C. E. Moore, Natl. Stand. Ref. Data Ser. **35**, Vol. I-III. Washington, DC: US GPO. See also the web site: www.nist.gov/pml/data/handbook/.

[21] C. J. Foot, *Atomic Physics* (Oxford University Press, Oxford, 2005); H. Friedrich, *Theoretical Atomic Physics* (Springer, Heidelberg, 2006).

[22] F. Herman and S. Skillman, *Atomic Structure Calculations* (Prentice-Hall, Englewood Cliffs, NJ, 1963).

[23] P. Hohenberg and W. Kohn, Phys. Rev. **136**, B864 (1964); W. Kohn and L. J. Sham, *ibid.* **140**, A1133 (1965).

[24] S. Kotochigova, Z. H. Levine, E. L. Shirley, M. D. Stiles, and C. W. Clark, Phys. Rev. A **55**, 191 (1997); **56**, 5191(E) (1997).

[25] J. F. Janak and A. R. Williams, Phys. Rev. B **23**, 6301 (1981).

[26] G. Lippert, J. Hutter, P. Ballone, and M. Parrinello, J. Chem. Phys. **100**, 6231 (1996).

[27] J. Vande Vondele and J. Hutter, J. Chem. Phys. **127**, 114105 (2007).

[28] The Coulomb potential from the nucleus is usually included in the external potential acting on the electrons. We instead include it in the Hartree potential in order to isolate in V_{ext} any static or time-dependent perturbation acting on the atom.

[29] J. P. Perdew and A. Zunger, Phys. Rev. B **23**, 5048 (1981).

[30] A. Stroud, *Approximate Calculation of Multiple Integrals* (Prentice Hall, Englewood Cliffs, NJ, 1971).

[31] S. H. Vosko, L. Wilk, and M. Nusair, Can. J. Phys. **58**, 1200 (1980).

[32] Beatings and chaotic behaviors could also result from several bound excited states. This case, however, does not seem to be relevant for the closed-shell atoms that we simulated, whose transitions all concern unbound states.

[33] S. J. A. van Gisbergen, F. Kootstra, P. R. T. Schipper, O. V. Gritsenko, J. G. Snijders, and E. J. Baerends, Phys. Rev. A **57**, 2556 (1998).

[34] M. E. Casida and D. R. Salahub, J. Chem. Phys. **113**, 8918 (2000).

[35] A. D. Becke, J. Chem. Phys. **98**, 5648 (1993).

[36] C. Adamo and V. Barone, J. Chem. Phys. **110**, 6158 (1999).

[37] R. T. Sharp and G. K. Horton, Phys. Rev. **90**, 317 (1953); J. D. Talman and W. F. Shadwick, Phys. Rev. A **14**, 36 (1976).

[38] P. Auger, J. Phys. Radium **6**, 205 (1925).

[39] A. Weiss, R. Mayer, M. Jibaly, C. Lei, D. Mehl, and K. G. Lynn, Phys. Rev. Lett. **61**, 2245 (1988); K. O. Jensen and A. Weiss, Phys. Rev. B **41**, 3928 (1990).

[40] A density functional strategy to define orbital energies in terms of KS orbitals and eigenvalues is discussed in M. Harris and P. Ballone, Chem. Phys. Lett. **303**, 420 (1999).

[41] M. Rohlfing and S. G. Louie, Phys. Rev. B **62**, 4927 (2000); E. L. Shirley and R. M. Martin, *ibid.* **47**, 15404 (1993); F. Bruneval, J. Chem. Phys. **136**, 194107 (2012).

[42] See, for instance, C. M. Isborn and X.-S. Li, J. Chem. Theory Comput. **5**, 2415 (2009).

[43] N. H. March, A. Rubio, and J. A. Alonso, J. Phys. B **32**, 2173 (1999).

[44] L. Bernasconi (private communication). Linear response computations carried out with the CRYSTAL code.